Air–water two-phase flow modeling of turbulent surf and swash zone wave motions

R. Bakhtyar [a,*], A.M. Razmi [a], D.A. Barry [a], A. Yeganeh-Bakhtiary [b], Q.-P. Zou [c]

[a] *Laboratoire de technologie écologique, Institut d'ingénierie de l'environnement, Faculté de l'environnement naturel, architectural et construit, Station 2, Ecole polytechnique fédérale de Lausanne (EPFL), CH-1015 Lausanne, Switzerland*
[b] *Enviro-Hydroinformatics COE, School of Civil Engineering, Iran University of Science and Technology, Tehran, Iran*
[c] *Centre for Coastal Dynamics and Engineering, School of Marine Science and Engineering, University of Plymouth, PL4 8AA, UK*

ABSTRACT

Wave breaking and wave runup/rundown have a major influence on nearshore hydrodynamics, morpho-dynamics and beach evolution. In the case of wave breaking, there is significant mixing of air and water at the wave crest, along with relatively high kinetic energy, so prediction of the free surface is complicated. Most hydrodynamic studies of surf and swash zone are derived from single-phase flow, in which the role of air is ignored. Two-phase flow modeling, consisting of both phases of water and air, may be a good alternative numerical modeling approach for simulating nearshore hydrodynamics and, consequently, sediment transport. A two-phase flow tool can compute more realistically the shape of the free surface, while the effects of air are accounted for. This paper used models based on two-dimensional, two-phase Reynolds-averaged Navier–Stokes equations, the volume-of-fluid surface capturing technique and different turbulence closure models, i.e., k–ε, k–ω and re-normalized group (RNG). Our numerical results were compared with the available experimental data. Comparison of the employed method with a model not utilizing a two-phase flow modeling demonstrates that including the air phase leads to improvement in simulation of wave characteristics, especially in the vicinity of the breaking point. The numerical results revealed that the RNG turbulence model yielded better predictions of nearshore zone hydrodynamics, although the k–ε model also gave satisfactory predictions. The model provides new insights for the wave, turbulence and means flow structure in the surf and swash zones.

1. Introduction

Control of coastal morphology has been identified as one of the most critical issues in coastal management. It is well known that predictions of hydrodynamics of surf and swash zones directly impact on predictions of sediment transport and thus on beach profile changes [1]. The complex nature of processes that occur in this area such as wave breaking and associated turbulence and mixed air–water flow requires an accurate description of the flow hydrodynamics. Indeed, laboratory studies indicate that the swash zone hydrodynamics are significantly affected by hydrodynamics and processes occurring in the breaking zone (inner surf zone) [2]. Therefore, for accurate modeling of hydrodynamic and sediment

* Corresponding author. Tel.: +41 21 693 8087; fax: +41 21 693 8035.
E-mail addresses: roham.bakhtyar@epfl.ch (R. Bakhtyar), amir.razmi@epfl.ch (A.M. Razmi), andrew.barry@epfl.ch (D.A. Barry), yeganeh@iust.ac.ir (A. Yeganeh-Bakhtiary), qingping.zou@plymouth.ac.uk (Q.-P. Zou).

dynamic processes in the swash zone, it is necessary to simulate both the wave breaking and swash zones.

Wave breaking and relevant hydrodynamic processes in the surf and swash zones have been studied by numerous investigators over the last two decades [3–5]. Vertical and horizontal velocities, turbulence characteristics as well as free surface tracking have been studied. In most cases numerical models were constructed based on the non-linear shallow water and/or Boussinesq equations [6,7]. Also, several hydrodynamic models based on the Reynolds-averaged Navier–Stokes (RANS) equations have been developed [1]. For example, Lin and Liu [8] developed a numerical model based on the NS equations to simulate breaking waves in the surf zone and found that the model results compared well with experimental data in the inner surf zone. Furthermore, the hydrodynamics of wave motion in the nearshore zone has been more thoroughly investigated, and several experimental studies have been done to perform quantitative analysis of the flow and turbulence characteristics.

Huang et al. [9] studied experimentally the turbulence dissipation rates and velocity fields of spilling breaking waves in the surf zone and mentioned that more studies were needed to elucidate energy transmission to the swash zone and bottom friction. Huang

Nomenclature

d	local still water depth (L)
E_i	experimental values
$\overline{E}_m$	experimental mean value
F	fluid volume ($L^3\,L^{-3}$)
g	magnitude of gravitational acceleration ($L\,T^{-2}$)
H	wave height (L)
k	turbulent kinetic energy ($L^2\,T^{-2}$)
L	wavelength (L)
N	number of observations
P	pressure ($ML^{-1}\,T^{-2}$)
P_i	predicted values
$\overline{P}_m$	predicted mean value
R^2	coefficient of determination
t	time (T)
T	wave period (T)
u_i	velocity component ($L\,T^{-1}$)
u^*	shear or frictional velocity ($L\,T^{-1}$)
x, z	horizontal and vertical coordinates, respectively (L)
X_s	surf zone width (L)

Greek

θ	bed slope
ρ_a	air density (ML^{-3})
ρ_w	fluid density (ML^{-3})
μ	molecular viscosity ($ML^{-1}\,T^{-1}$)
σ_{ij}	strain rate tensor ($L^{-1}\,T^{-1}$)
$\overline{\tau}_{ij}^m$	average stress tensor ($ML^{-2}\,T^{-2}$)
v_a	kinematic viscosity of air ($ML^{-1}\,T^{-1}$)
v_w	kinematic viscosity of water ($ML^{-1}\,T^{-1}$)
v_t	eddy viscosity ($L^2\,T^{-1}$)
ε	turbulence dissipation rate ($L^2\,T^{-3}$)
κ	von Kármán constant
ω	specific dissipation rate ($L^2\,T^{-3}$)
ζ	surf similarity parameter
Γ_k, Γ_ω	effective diffusivity of k and ω, respectively ($ML^{-1}\,T^{-1}$)
Δt	time step (T)
$\sigma_k, \sigma_\varepsilon, C_{1\varepsilon}, C_{2\varepsilon}, C_\mu$	empirical constants

Subscripts

b	breaking point value

et al. [10] measured the wave bottom boundary layer velocity in the surf zone using particle image velocimetry and observed that a notable number of intermittent turbulent eddies penetrated into the wave bottom boundary layer. In the surf and swash zones, Sou et al. [11] investigated the velocity and turbulence fields under plunging breaking waves. Shin and Cox [12] provided a comprehensive, accurate data set of horizontal and vertical velocities and investigated the structure of undertow, free surface, turbulence intensity and energy.

In order to analyze water free surface flow, it is of course important to determine the position of free surface as it varies temporally. In such flows, in addition to the velocity, pressure and turbulence fields, the location of the free surface is one of the major unknowns [13]. There are two viewpoints for tracking the water free surface, namely: Lagrangian and Eulerian. In the former, water particle movement near the free surface is determined based on the local flow velocity. In the latter, the temporal variation of the free surface at a given location is computed. The Eulerian perspective is more compatible with the NS equations, and is the basis of volume-of-fluid (VOF) technique [13], which will be used subsequently.

In the VOF technique [14], the volume fraction, F, of the computational cell occupied by the fluid determines the free surface. The free surface is defined for cells in which F is between zero and unity and there is at least one adjacent cell with a volume fraction of zero. The derivatives of F can be used to define the fluid location in any cell. From the derivatives of F, the direction in which the variation of F is faster is defined and hence the vector normal to the free surface. In addition, from the surface tension, the curvature of the free surface is defined. Fig. 1 shows how VOF technique approximates the free surface.

Bradford [15] proposed a numerical solution of the NS equations in conjunction with the VOF method and investigated the applicability of different turbulence closure models for modeling breaking waves in the nearshore zone. Zhang and Liu [16] simulated dam break-generated bores, propagating, runup and rundown over a sloping beach. Christensen and Deigaard [17] and Christensen [18] used the NS equations in conjunction with large eddy simulation (LES) to simulate the plunging and spilling breaking waves. A two-dimensional multi-scale turbulence model using the VOF method for modeling breaking waves was proposed by Zhao et al. [19]. These models considered single-phase water flow, not combined air and water flow.

Bakhtyar et al. [20] presented a two-dimensional numerical model for simulation of wave breaking, turbulence, undertow current and wave characteristics in the surf and swash zones. Their model is based on the Reynolds-averaged Navier–Stokes (RANS) equations, VOF and a k–ε turbulence model. The model was used to investigate overturning, uprush and backwash of waves on the beach slope. Bakhtyar et al. [21–23] developed a two-phase flow model to analyze numerically sheet flow, sediment transport under the influence of wave breaking, and wave runup in the surf and swash zones. Their results explored different wave, beach and sediment conditions, but did not consider the effects of air entrainment during wave motion.

Entrapped air bubbles may have significant impacts on surf and swash zone hydrodynamics processes such as wave breaking, run-up/down and momentum exchange. Air–water two-phase flow is not well understood, and so there is a need for further investigation into the details of this type of flow. Most previous numerical investigations focused on the water motion and neglected the effect of the water–air mixing process. Air–water two-phase flow modeling has been reported in the context of coastal engineering. Hieu and Tanimoto [24] developed a two-phase flow model for simulation of wave transformations in shallow water and over a
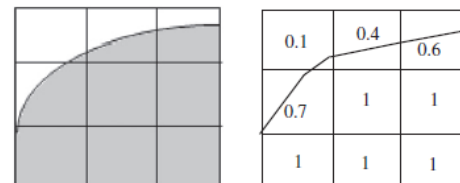

Fig. 1. Free surface approximation using the VOF method. Left panel shows the actual interface between the air and water phases, while the right panel represents the volume fractions associated with the interface using the VOF technique.

submerged obstacle, while Karim et al. [25] developed a two-phase model for simulation of waves in a vertical permeable structure. They used LES to model turbulent flow, and thereby characterized the effect of small-scale turbulence. Hieu et al. [26] proposed a numerical two-phase flow model together with the volume tracking method for incompressible viscous fluids, and used it to simulate wave propagation and air movement. Their results confirmed that the two-phase flow model is a powerful tool for the simulation of wave propagation in shallow water. They used the sub-grid scale turbulent Smagorinsky model for turbulence and eddy viscosity estimation. Lubin et al. [27] developed a numerical model to investigate plunging breaking waves by solving the NS equations, in air and water, coupled with a dynamic sub-grid scale turbulence model. They concluded that further studies would be necessary to advance the modeling of turbulence and so increase the flow description accuracy. Hieu and Tanimoto [28] presented a VOF two-phase flow model for the simulation of wave and porous structure interactions and again employed the sub-grid scale turbulent Smagorinsky model. Their results confirmed that the two-phase flow model is a valuable tool for the analysis of interactions between waves and porous structures. Recently, Wang et al. [29] used a two-phase flow model to simulate spilling breaking waves in the surf zone and found that the calculated breaking point location, averaged surface elevations and undertow were in good agreement with laboratory measurements. However, turbulence models were not closed explicitly in their model and it could be improved to account for two-phase turbulence modeling.

Additional description and discussion of the mathematical modeling approaches that have been used to simulate wave motion in the surf and swash zones were summarized by Brocchini and Baldock [30] and Bakhtyar et al. [1]. Existing two-phase numerical models cannot fully describe the spatial and temporal envelope of the flow and turbulence structures of the combined surf and swash zones. Especially, the two-phase flow approach has not been well validated with experimental data in the swash zone. In addition, the turbulence in the inner surf and swash zones has not been well captured by previous two-phase flow models. Further studies are needed to clarify the detailed characteristics of two-phase flow and especially the turbulence structure in the swash zone. In this study, the nearshore hydrodynamics were simulated using a two-phase flow model, which solves the two-dimensional RANS equations. In order to capture accurately the air–water interface, we adopted the VOF technique. Indeed, an important feature of the present model is its capability of handling density differences between air and water in the free surface and accounting for the mixing of air and water. In this context, the k-ε, k-ω and RNG turbulent closure models were used to predict the turbulent stresses.

This paper is composed of five sections. Section 2 gives the mathematical formulation for the two-phase flow model. In Section 3, we compare the numerical results with the experimental measurements of Shin and Cox [12] and Shin [31] for the surf and swash zones. Furthermore, this section presents the flow and turbulence structures, and the results of numerical experiments conducted to investigate the effects of wave breaking on the nearshore hydrodynamics. Finally, conclusions are presented in Section 4.

2. Hydrodynamic model

A numerical solution to the two-phase air–water equations based on an Eulerian–Eulerian scheme was employed. In the Eulerian framework, the two phases are considered as separate media, while the governing equations of motion for each phase are coupled and then solved. Conservation equations for each phase were derived to produce a set of equations having a similar structure for each phase. The equations for both phases (air and water) were supplemented with an additional equation that computes the volume fraction of the phases at the free surface. Therefore, the variables and properties in each cell are either only representative of one of the phases, or representative of a mixture of the phases, depending upon F at a given location.

2.1. Governing equations

The mathematical description of non-linear waves involves the unsteady NS equations in two (cross-shore) dimensions. Air and water are assumed to be incompressible without inter-phase transfers or phase changes. The motions of both fluids (water and air) are described by the NS equations [32]. In the surf and swash zones, where turbulent flows with high Reynolds numbers exist, the turbulent oscillations make the direct numerical simulation of these equations to be difficult and CPU intensive. An alternative method for the analysis of turbulent flows is to consider the average motions of the flow and to evaluate the effects of turbulent oscillations on the average motion. For this reason, we consider the velocity and pressure fields as the sum of the mean and fluctuating parts. By implementing the Reynolds decomposition in the NS equations and averaging, the Reynolds-Averaged Navier–Stokes (RANS) equations governing the average flow field are derived:

$$\frac{\partial \bar{u}_i}{\partial x_i} = 0, \tag{1}$$

$$\frac{\partial \bar{u}_i}{\partial t} + \bar{u}_j \frac{\partial \bar{u}_i}{\partial x_j} = -\frac{1}{\rho}\frac{\partial \overline{P}}{\partial x_i} + g_i + \frac{1}{\rho}\frac{\partial \bar{\tau}_{ij}^m}{\partial x_j} - \frac{\partial \overline{u_i' u_j'}}{\partial x_j}, \tag{2}$$

where $\tau_{ij}^m = 2\mu\bar{\sigma}_{ij}$ is the average stress tensor, $\bar{u}_i$ is the average velocity component, P is the pressure; ρ is the density, g is the magnitude of gravitational acceleration, and $\bar{\sigma}_{ij}$ is the average strain rate tensor. The term $-\frac{\partial \overline{u_i' u_j'}}{\partial x_j}$ represents the effects of the turbulent flow on the mean flow field and $-\overline{u_i' u_j'}$ is the stress tensor. In the above equations, the number of unknown variables is more than the number of equations, and further equations are required, which relate the Reynolds stresses to the known variables. These auxiliary equations are given by turbulent closure models. In this study, three different closure models were used, namely the k-ε, k-ω and RNG models, where k is the turbulent kinetic energy (TKE); ε is the turbulence dissipation rate; and ω is the specific dissipation rate. A detailed description of the different turbulence closure models is given in Appendix A.

The system of two-phase flow equations consists of the conservation of mass, horizontal and vertical momentum equations, turbulence closure model, VOF equation, and variation of density and viscosity for the two-phase flow model. In other words, the model accounts for the effects of air entrainment on the wave hydrodynamics. This makes the numerical model suitable for predicting the wave free surface in the nearshore zone as well as other flow characteristics. The VOF, density and viscosity models employed are, respectively:

$$\frac{\partial F}{\partial t} + \bar{u}_i \frac{\partial F}{\partial x_i} = 0, \tag{3}$$

$$\rho = (1-F)\rho_a + F\rho_w, \tag{4}$$

$$\mu = (1-F)\mu_a + F\mu_w, \tag{5}$$

where ρ_w and ρ_a are the water and air densities, respectively; μ_a and μ_w are the molecular viscosity of water and air, respectively. The behavior of density and viscosity inside the computational cells was characterized by Eqs. (4) and (5). These terms reduce, as appropriate, to the expressions for the single phases (e.g., water ($F = 1$, $v = v_w$, $\rho = \rho_w$) and for air ($F = 0$, $v = v_a$, $\rho = \rho_a$)).

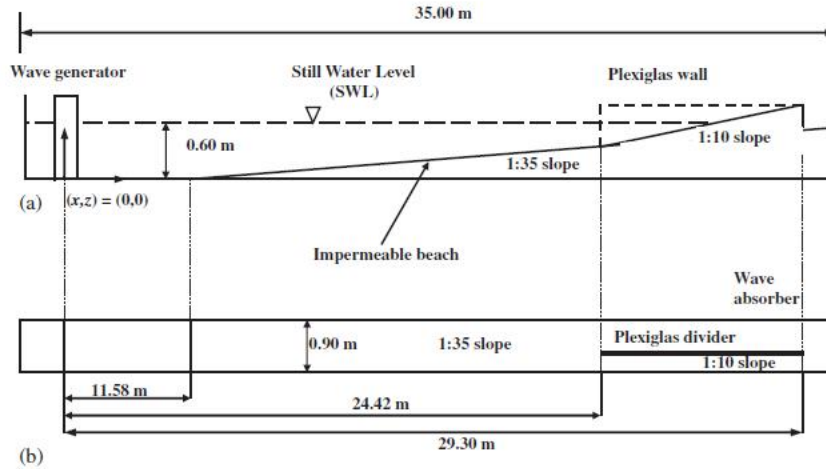**Fig. 2.** Sketch of wave flume and experimental setup [12,31]: (a) side view; (b) plan view (after [2]).
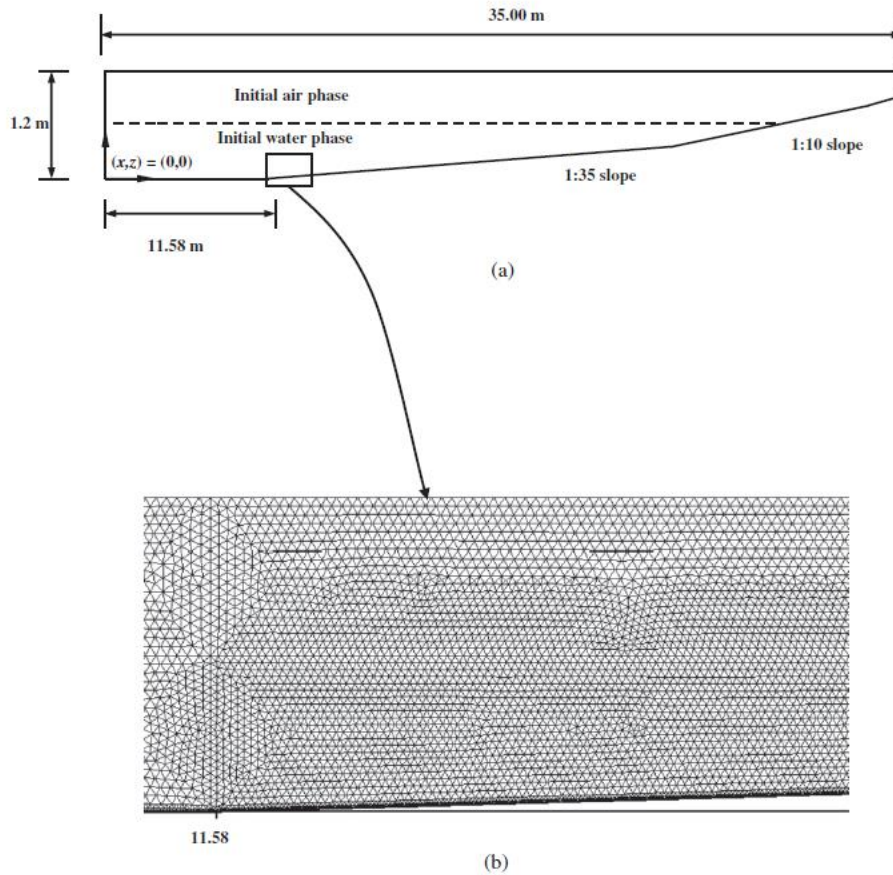

Fig. 3. (a) Computational domain, (b) an example of the numerical grid that was used for the two-phase flow model. (b) The grids near the beach toe. The grids consisted of unstructured non-uniform triangular cells. The sizes of grids near the boundaries, air–water interface and in the swash zone were finer than elsewhere.

2.2. Initial and boundary conditions

All forms of fluid flows are expressed with a single type of differential equation (NS equations) and only of the boundary and initial conditions are different. The different types of boundary conditions not only influence the numerical stability, but also affect the accuracy of numerical solutions.

Zero velocities of the flow field together with a hydrostatic pressure distribution were used as the initial conditions. At the bottom, the no-slip boundary condition was applied together with a zero

normal velocity component. For near-wall turbulent quantities, the log-law velocity in the turbulent boundary layer is expressed as

$$\bar{u} = u_* \kappa^{-1} \ln(9.8 u_* z \nu^{-1}), \qquad (6)$$

where $u_* = (\tau_w \rho^{-1})^{\frac{1}{2}}$ is the wall shear velocity; z is the distance from the bed; τ_w is the shear stress in the flow direction and $\kappa = 0.41$ is the von Kármán constant.

The inlet boundary condition consisted of the time-dependent surface elevation, vertical and horizontal velocity components. These were based on the characteristics of the different wave types considered. The pressure outlet (gauge pressure) boundary condition was applied at the land boundary.

2.3. Numerical scheme

The simulation was carried out using the FLUENT software, in which the two-dimensional equations were discretized by the finite-volume approach with unstructured non-uniform triangular cells. The grid consisted of two zones, the air and the water. Generally, the size of grids in the air phase was greater than the liquid phase. In addition, we used a finer grid near the boundaries, air–water interface and in the swash zone. A second-order upwind scheme was used to discretize the governing equations, while quantities at cell faces were computed using a multi-dimensional linear reconstruction approach [33]. In this approach, higher-order accuracy is achieved at cell faces through a Taylor series expansion of the cell-centered solution about the cell centroid. For pressure–velocity coupling, the computationally efficient pressure-implicit with splitting of operators (PISO) was used. Temporal discretization of the governing equations was accomplished by an implicit time-marching scheme [34]. Stability was controlled mainly by the value of Δt (time step), i.e., the local Courant number, which varies with the local flow behavior. These schemes ensured satisfactory accuracy and stability. During the solution process, the convergence was controlled dynamically by checking residuals. At the end of each solver iteration, the residual sum for each of the conserved variables was computed. These residuals go to zero as the solution converges.

3. Results and discussion

The problem investigated here is treated as a two-phase model, the upper phase is air and the lower phase is water. In this section, results of our numerical model are compared with experimental

data. The simulated velocity field, wave properties, and the spatial and temporal distributions of turbulence characteristics such as TKE, turbulent dissipation rate and eddy viscosity in the nearshore are presented and discussed.

3.1. Validation of the two-phase flow model

The model results were compared with the experimental data of Shin and Cox [12] and Shin [31]. A schematic configuration of

Fig. 4. Cross-shore variation of water depth in the nearshore zone using the (a) k–ω, (b) k–ε, and (c) RNG models. Empty circles are the experimental data [12,31] and solid lines are the numerical results.

Table 1
Characteristics of wave conditions in the experiments of Shin and Cox [31].

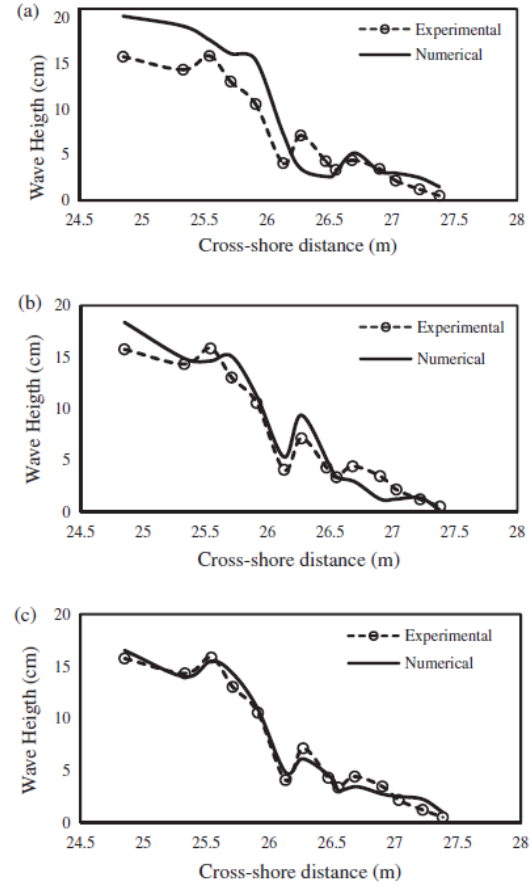| T (s)	H_0 (cm)	H_b (cm)	h_b (cm)	X_s (m)	ζ
2.00	12.16	15.67	12.10	1.21	0.63

Table 2
Statistics of experimental data and numerical predictions of hydrodynamic characteristics in the nearshore zone.

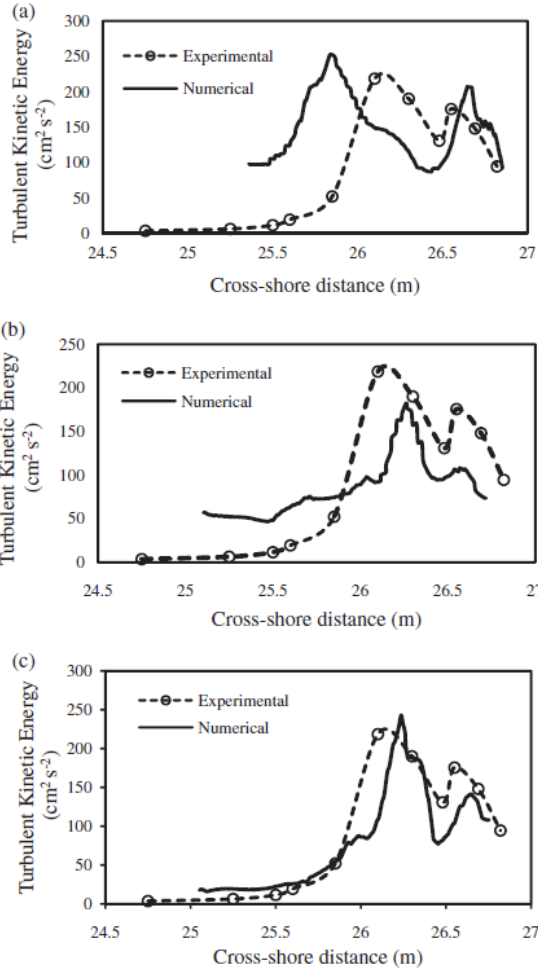| Hydrodynamic variable	Numerical model	Averaged experimental values	Averaged numerical predictions	SI (%)	RMSE	bias	R^2
Wave height (cm)	k–ω	7.13	8.60	39.55	2.82	1.47	0.95
	k–ε	7.13	7.43	19.19	1.37	0.30	0.97
	RNG	7.13	7.26	9.67	0.69	0.08	0.99
TKE (cm^2 s^{-2})	k–ω	104.1	131.82	76.21	79.34	21.72	0.28
	k–ε	104.1	86.92	49.44	51.37	−16.98	0.83
	RNG	104.1	93.62	24.53	25.74	−11.34	0.95
Undertow (cm s^{-1})	k–ω	−10.95	−13.83	−50.28	5.51	−2.88	0.72
	k–ε	−10.95	−12.5	−37.64	4.12	−1.55	0.84
	RNG	−10.95	−12.37	−33.53	3.65	−1.43	0.86

Fig. 5. Cross-shore variation of TKE in the nearshore zone using the (a) $k-\omega$, (b) $k-\varepsilon$, and (c) RNG models. Empty circles are the experimental data [12,31] and solid lines are the numerical results.

Fig. 6. Cross-shore variation of mean velocity (undertow) near the bed (0–0.4 cm above the bed) using the (a) $k-\omega$, (b) $k-\varepsilon$, and (c) RNG models. Empty circles are the experimental data [12,31] and solid lines are the numerical results.

their experimental setup and wave flume are shown in Fig. 2. The 29.3-m flume was filled with fresh water to a maximum depth of 0.60 m. The beach had two different slopes with an impermeable bed. The former slope was 1:35 starting at $x = 11.58$ m followed by a 1:10 slope at $x = 22.42$ m. A regular wave with 2.0 s period was generated, while the reference wave height was 11.38 cm.

We investigated the model's grid convergence ensure that the computational results are grid independent. To achieve this, different sets of grids with different sizes and shapes (triangular and rectangular) were used. Based on the computational run time and convergence rate, non-uniform triangular grids with sizes between 0.0075 and 0.04 m were selected. This grid system gave negligible differences when compared with the finer mesh results. Fig. 3 shows the numerical grids in the computational domain with different sizes. The initial time step was $\Delta t = 10^{-3}$ s, which was reduced to 10^{-6} s during the calculations to satisfy the stability and convergence constraints. The model used small time steps only near wave breaking. Moreover, in our computations, in order to reduce the computational effort, we did not calculate the wave propagation for the entire experimental period, which would have

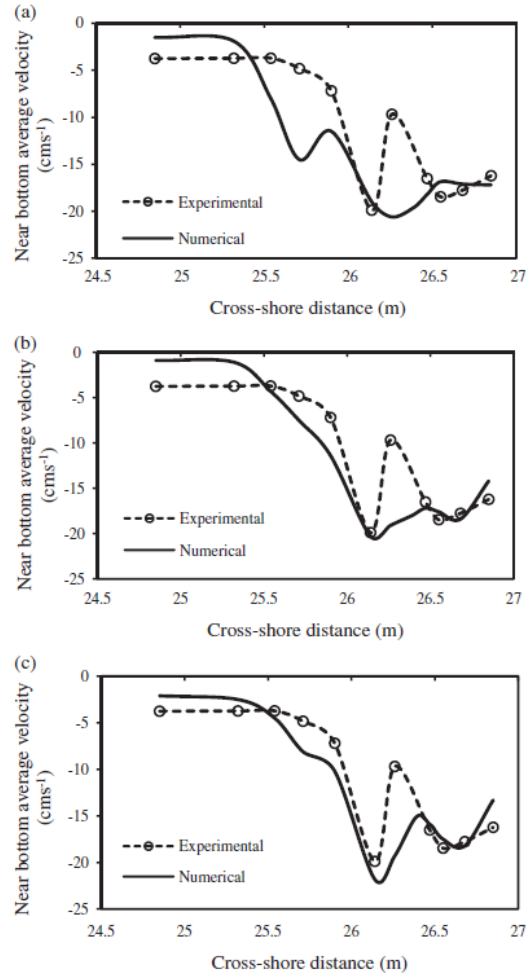required a very huge CPU time. Instead, numerical solutions presented herein are from $t = 18$ to 20 s. This particular initial time ($t = 18$ s) matches with the time $t/T = 0$ in the phase-averaged results where T is the wave period. The computed results for the mean velocities and free surface profiles indicate that the computed waves in surf zone reached quasi-steady state, i.e. there is a very small difference between two successive wave cycles. Table 1 reports the parameters describing the incident wave conditions, where H and L are the wave height and wavelength, respectively; d is the local still water depth and the subscripts 0 and b denote respectively the deep-water and wave breaking conditions. ζ is the surf similarity parameter characterizing the type of wave breaking and hydrodynamics of the nearshore zone; it is defined as [35]:

$$\zeta = (L_0 H_0^{-1})^{\frac{1}{2}} \tan \theta, \quad L_0 = gT^2(2\pi)^{-1} \tag{7}$$

in which θ is the beach slope. As shown in Table 2, $\zeta = 0.63 > 0.5$ indicates that plunging breakers occur. The density and viscosity

of air were $1.225\,\mathrm{kg\,m^{-3}}$ and $1.789 \times 10^{-5}\,\mathrm{Pa\,s}$, respectively. The kinematic viscosity of water was $10^{-6}\,\mathrm{m^2\,s^{-1}}$. At the start of each numerical simulation, the location of the air–water interface was set at the horizontal line from the intersection of the SWL and slope to the inlet boundary (Fig. 3a). All of the results presented in the figures are for the water phase.
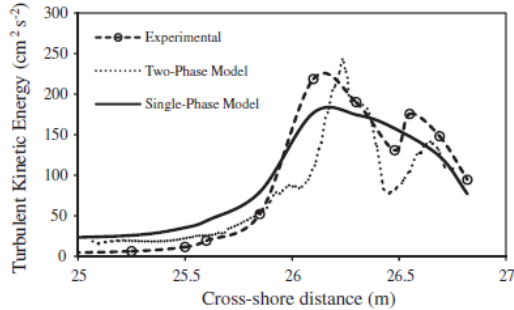

Fig. 7. Cross-shore variation of TKE in the nearshore zone using the single-phase and two-phase flow models. Empty circles are the experimental data [12,31].

The cross-shore variation of wave height for both measured and simulated results are shown in Fig. 4, which shows the numerical results of two-phase flow using the k–ε, k–ω and RNG turbulence closure models. The simulation results are in good agreement with the experimental data. The experimental results show that the wave breaks twice at $x = 25.54\,\mathrm{m}$ and $x = 26.46\,\mathrm{m}$ (Fig. 4 and [12]). Numerical predictions of the breaking points match well the experimental results. For a statistical comparison of the numerical results and experimental data, the *bias* (mean error), the scatter index (*SI*), and the root mean square error (*RMSE*) were calculated. Expressions for these statistics are shown in Appendix B. Table 2 shows the statistics of observed wave height and the values of predicted wave heights using the k–ε, k–ω and RNG models. It can be seen that for each turbulence model the wave height is over-predicted (*bias* = 0.30 cm, 1.47 cm and 0.08 cm for the k–ε, k–ω and RNG models, respectively). In addition, the *SI* for the k–ω model (*SI* = 39.55%) is larger than those for the k–ε and RNG methods (*SI* = 19.19% and 9.67%). Moreover, the values of the coefficient of determination (R^2) of the RNG model (0.99) is higher than that for the k–ε (0.97) and k–ω (0.95) models, while the *RMSE* of the RNG model (0.69 cm) is significantly lower than that for other models (2.82 and 1.37 cm for k–ω and k–ε, respectively). Generally, the results (Fig. 4 and Table 2) suggest that the two-phase flow
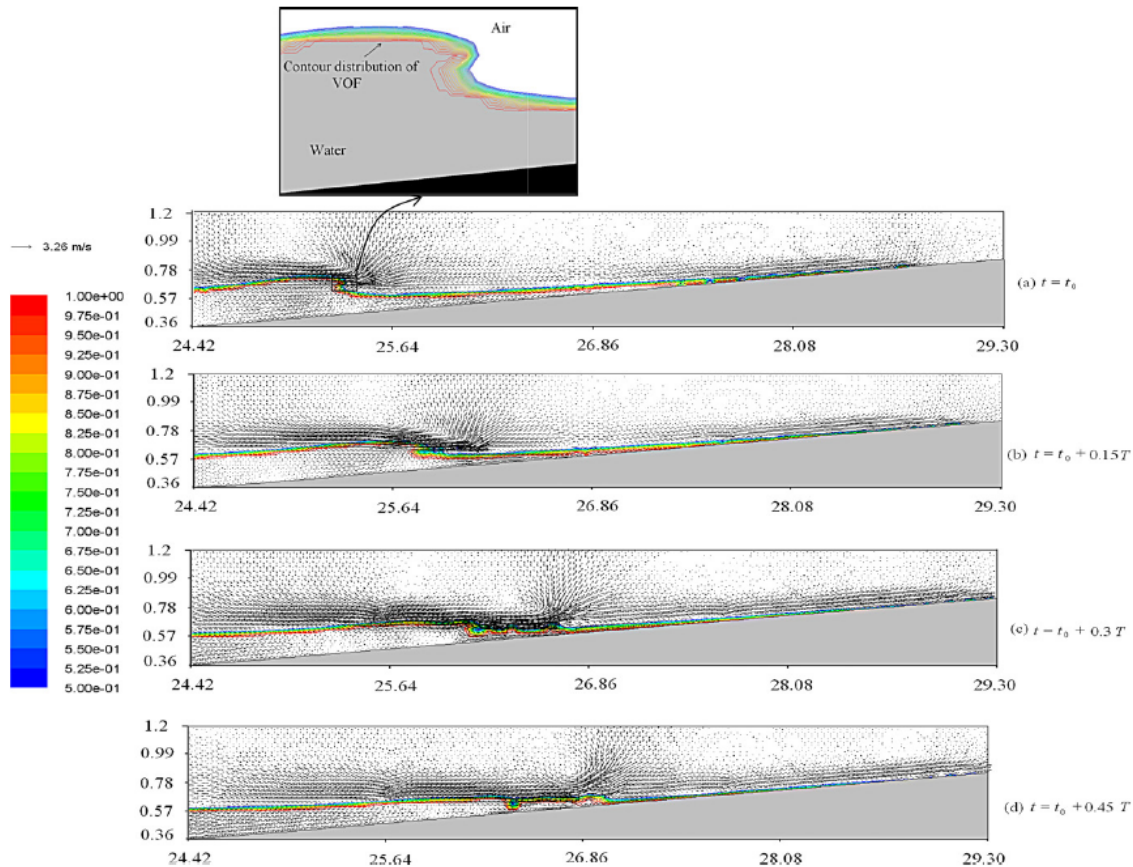

Fig. 8. Water surface elevations (F contours), wave motion and velocity vectors in the nearshore zone at different times. In all panels, the horizontal axis shows the cross-shore distance in m, the vertical axis shows the vertical distance in m, and the length of the vectors is proportional to the magnitude of velocity. Velocity units are in m s^{-1} and the contour bar shows the values of F at the interface of water and air (between zero and unity). t_o is equal to 18 s.

method (especially using the RNG scheme) predicts satisfactorily the wave height in surf and swash zone.

To further understand the physical behavior and validate the numerical results presented in this study, we consider next the simulation of turbulence in nearshore environments. Fig. 5 depicts the cross-shore variation of the TKE (summation of cross sectional TKE at any cross-shore distance) for both of the experimental data and numerical results (using the three turbulence closure models) in the nearshore zone. Before the breaking zone, all models over-estimate the experimental results. The discrepancies between numerical and experimental results are likely due to the fact that the generation and transformation of bed friction-induced turbulence is not modeled properly [20]. However, from the breaking point to the swash zone, the results of the k–ε and RNG models are less than the experimental observations, while those of the k–ω model are higher. The results show that the maximum TKE occurs after the breaking point under the plunging breaker and inside the surface roller. The strong turbulence generated by the plunging breaker is advected into the swash zone and decreases the undertow. After the breaking point, the TKE decreases towards the shore. The panels of Fig. 5 show two peaks corresponding to the two breaking points. The TKE in the zone between two of the breaking points is at least an order of magnitude greater than that in the outer surf zone mainly because the turbulent production is intensified in the former. The k–ε and RNG models both predict well the position of the breaking points. In contrast, the k–ω model predicted the breaking points earlier than observed.

The statistics of observed wave-induced TKE and also the magnitudes of predicted TKE using k–ε, k–ω and RNG models are given in Table 2. As seen there, both the k–ε and RNG models underpredict the TKE (bias = −16.98 cm^2 s^{-2} and −11.34 cm^2 s^{-2}, respectively), while the two-phase flow model using the k–ω closure model over-predicted the TKE (e.g., bias = 21.72 cm^2 s^{-2}). The SI for the k–ω model predictions (SI = 76.21%) is much larger than those of the k–ε or RNG models (SI = 49.44% and 24.53%, respectively). The values of the coefficient of determination of the two-phase flow model with RNG closure are higher than for the other models, while its RMSE is lower. The results suggest that the RNG model is more capable than the k–ε model in simulating the TKE and that both perform much better than the k–ω model. The improvement in the RNG model over the k–ω model may be due to the constants used in the latter, which were calibrated from the homogeneous turbulence production [36] and might not be suitable for the surf and swash zones. Another possible reason may be related to the imposition of the wall function at the bottom boundary derived from the fully developed plane boundary layer flow, and is well known for its poor performance in resolving the disequilibrium between turbulence generation and dissipation in this area. Furthermore, the k–ω turbulence cannot predict (accurately) the TKE in areas with strong acceleration like the inner surf and swash zones, where it over-predicts the experimental results. The main sources for disagreement between numerical results and experimental data were discussed in detail in Bakhtyar et al. [20].

In the nearshore zone, especially in vicinity of the breaking points, the variation of cross-shore velocity with depth cannot be ignored. The shoreward mass transport by the breaking waves in a surf zone has to be compensated by a seaward return flow, the undertow [37]. Svendsen's [37] theory suggest that the undertow
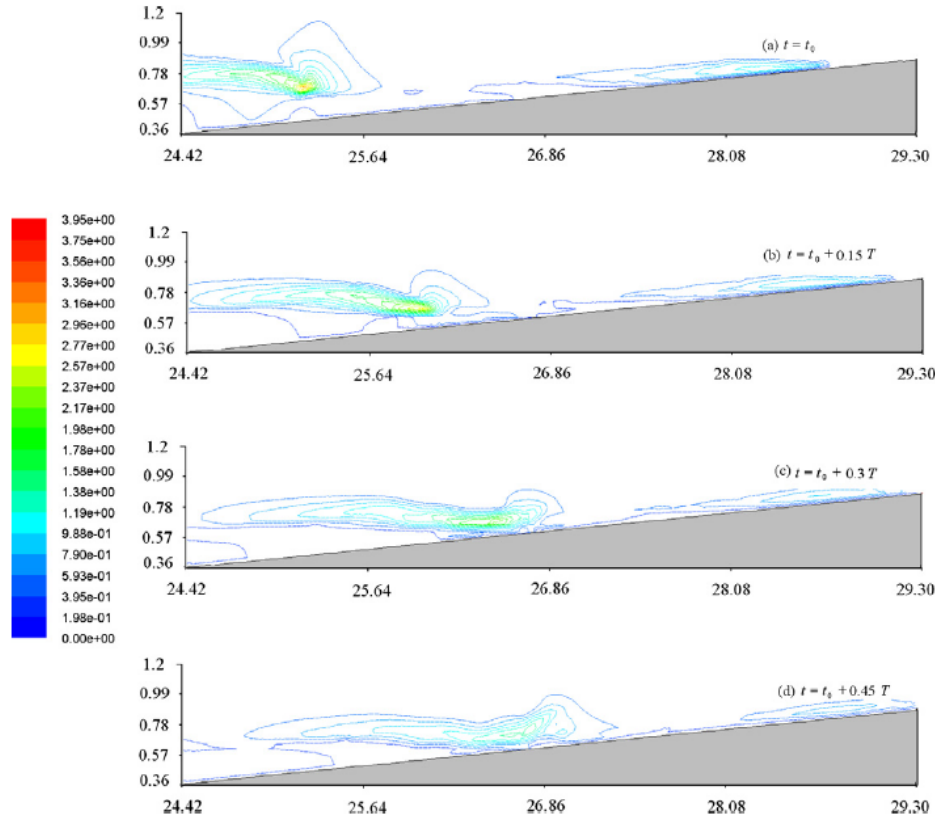

Fig. 9. Snapshots of distribution of velocities near the breaking point. The horizontal and vertical axis shows the cross-shore distance on the 1:10 slope in m and vertical distance in m, respectively. Velocity units are in ms^{-1}.
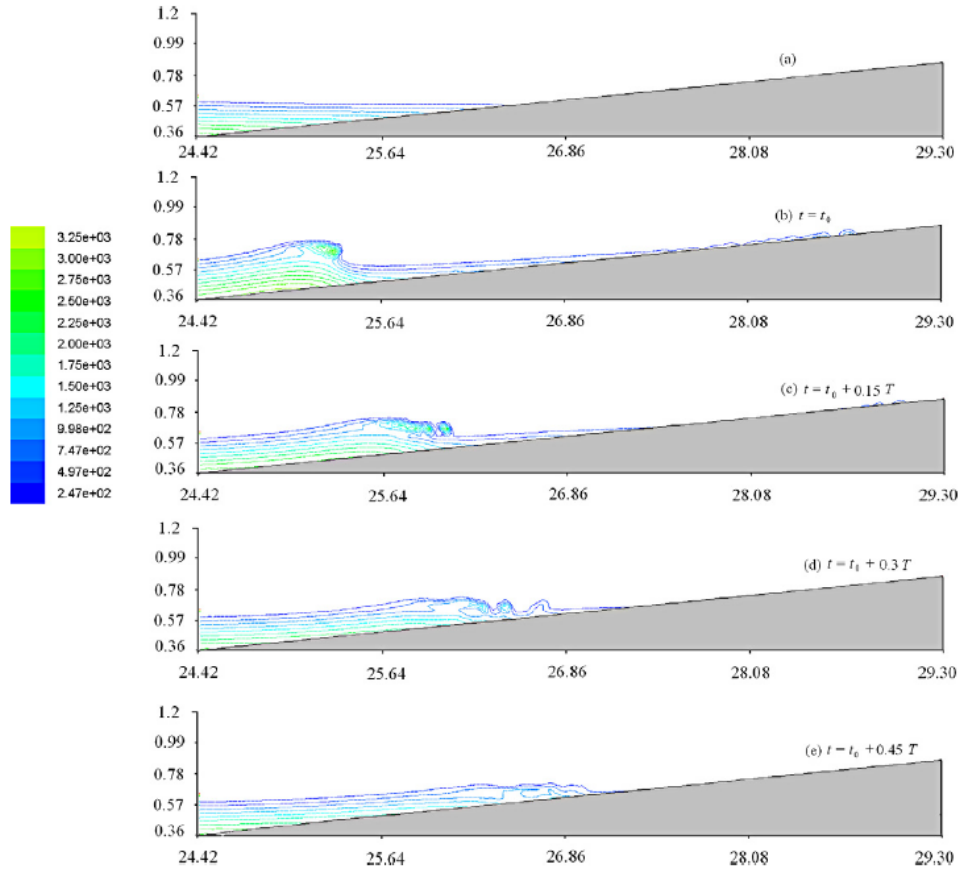
Fig. 10. Contours of the total pressure under wave motion. The horizontal axis shows the cross-shore distance in m, and the vertical axis shows the vertical distance in m. Panel (a) shows the distribution before reaching wave, while panels (b–e) show the pressure near the wave breaking. Pressure units are in Pa.

is driven by the local difference between wave radiation stress and the setup pressure gradient and that turbulent shear stresses are required to maintain a steady situation [37]. Fig. 6 compares the nearshore mean horizontal velocity (undertow) near the bed for the experimental data and different types of numerical modeling. Before the first breaking point, the magnitude of the undertow velocity is low, offshore and constant. After the breaking points, two strong offshore flows are apparent and the undertow value is reduced in the swash zone and towards the shore. According to the experimental results, the maximum undertow values are located at $x = 26.14$ and 26.55 m. Both the $k–\varepsilon$ and RNG models are capable of qualitative simulation of the points corresponding to the greatest undertow magnitudes. In general, the trend of wave height, undertow and TKE were simulated very well. In other words, after the last point of wave breaking, the height of the water column reaches its maximum, while the undertow is rather uniform. In the swash zone, a local minimum of incident wave height, setup and undertow can be seen. This behavior may be due to the fact that the maximum turbulence in the flow field and near bed occurs ($x = 26.5$ m) and this turbulence induces the undertow decrease. Fig. 6 demonstrates that the $k–\omega$ and $k–\varepsilon$ turbulence closure models produce high undertow estimates especially near the breaking points (from $x = 25.6$ to 26.5 m), while the RNG model provides higher accuracy for undertow prediction than the other models. All models show less satisfactory performance in the roller region, where there is higher velocity and momentum exchange. In the rest of nearshore zone, all models show much better performance in predicting the undertow rather than the region close to the breaking points. The numerical results reveal that, for the three turbulence closure models considered, the two-phase flow model can predict well the undertow.

Table 2 reports the statistics of observed and predicted undertow using two-phase flow with the $k–\varepsilon$, $k–\omega$ and RNG models. All the models give a higher undertow ($bias = -2.88$, -1.55 and -1.43 cm s^{-1} for the $k–\omega$, $k–\varepsilon$ and RNG turbulence models, respectively) in the nearshore zone. Furthermore, the SI for the $k–\omega$ model ($SI = 50.28\%$) is larger than that of the $k–\varepsilon$ and RNG methods ($SI = 37.64\%$ and 33.53%). The $RMSE$ between the measured and calculated undertow velocity using $k–\omega$, $k–\varepsilon$ and RNG models are 5.51, 4.12, and 3.65 cm s^{-1}, respectively. The coefficient of determination between the measured and simulated near bottom undertow for $k–\omega$, $k–\varepsilon$ and RNG models are 0.72, 0.84, and 0.86, respectively, showing that the present two-phase flow model can represent accurately the trend of mean flow velocity in the surf and swash zones.

Besides the experimental data, we also compared our model results with those of the single-phase flow model of Bakhtyar et al. [20]. Fig. 7 shows the cross-shore variation of the TKE for both of the experimental data and numerical results (using the single-phase and two-phase flow models) in the surf and swash zones. Before the breaking point, both models slightly over-estimate the TKE in the surf zone, while the accuracy of two-phase flow model
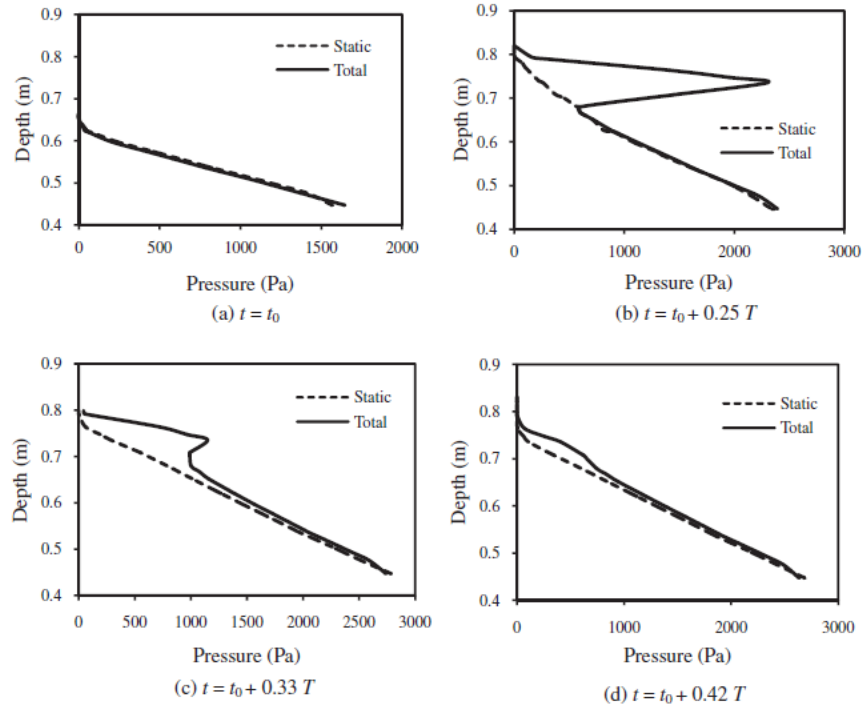
Fig. 11. Vertical total and static pressure distributions at different times near the breaking point.

is higher. The two-phase flow model results show that the wave breaks twice that in an agreement with experimental data. The single-phase flow model, on the other hand, shows one breaking point. As in the nearshore zone, there is significant mixing of air and water with relatively high TKE, so prediction of the free surface needs to incorporate the effects of air on the hydrodynamics. Therefore, the two-phase flow model gives a better estimation of the TKE behavior, although the single-phase model also gives satisfactory predictions.

The results given in Figs. 4–7 showed that, by using the different turbulence closure models, various numerical results might be attained for the nearshore hydrodynamic characteristics. This suggests that, for a realistic prediction, the numerical model must account for the TKE induced in the water column. The RNG model gives more realistic results than the other two models. Therefore, in the rest of present paper, we use the two-phase flow approach supplemented with the RNG turbulence closure model.

3.2. Wave motion and flow structure

The incident waves are the most important energy source for beach evolution and sediment transport towards the offshore, onshore or along the beach. In order to improve understanding of nearshore behavior, it is necessary to investigate the wave propagation, shoaling, breaking and runup/down in the surf and swash zones. The time evolution of the water surface elevation (contour distribution of the F) and wave motion over the bed slope and the averaged flow velocity field in the surf and swash zones are shown in Fig. 8 (note that the length of the arrows is proportional to the velocity magnitude). Fig. 8 shows the results in the cross-shore area from $x = 22.4$ to 29.3 m (on the 1:10 bed slope). As the non-linear wave approaches the shoreline, the wave profile grows steeper and the water depth decreases progressively. This steepness contin-

ues until the waves break (Fig. 8a,b). Waves that reach the beach areas dissipate much of their energy as turbulence-induced heat, and movement of water caused by wave breaking, friction and penetration towards the bed. After wave breaking, the mixing rate increases, wave height decreases and wave runup starts (Fig. 8c), followed by rundown. At the end of wave rundown, the subsequent incident wave reaches the shore. Therefore, there is often interaction between the subsequent incident wave and the rundown of the former incident wave. Panel (d) shows this interaction after one swash cycle and illustrates that the maximum velocity takes place near the beginning point of runup motion ($x \sim 28.8$ m).

Fig. 9 gives snapshots of the velocity distribution in the cross-shore direction on the 1:10 slope. It is evident that the liquid velocity in both horizontal and vertical directions changes with depth and time. It can be seen from Fig. 9 that the flow velocity increases rapidly near the breaking points, and maximum cross-shore velocity is in excess of 3.7 cm s^{-1}. The large magnitude of the flow velocity in the surface free water is shown in Fig. 8. Before the breaking point, the wave motion is irrotational (i.e., orbital wave motion does not distorted). Panels (b) and (c) show the breaking and collapsing of waves on the beach slope, in which the upper portion of the flow has a higher velocity than the lower part. Panel (c) shows the velocity after breaking. It indicates the early stages of wave runup that later becomes the runup/down evident in panel (d).

3.3. Pressure distribution

The total pressure distribution of the non-linear shoaling wave is shown in Fig. 10. Panel (a) shows the pressure distribution before the incident wave reaches the nearshore zone. The contours are horizontal, i.e., the pressure distribution is hydrostatic. When the waves reach to the surf zone and before the breaking point,
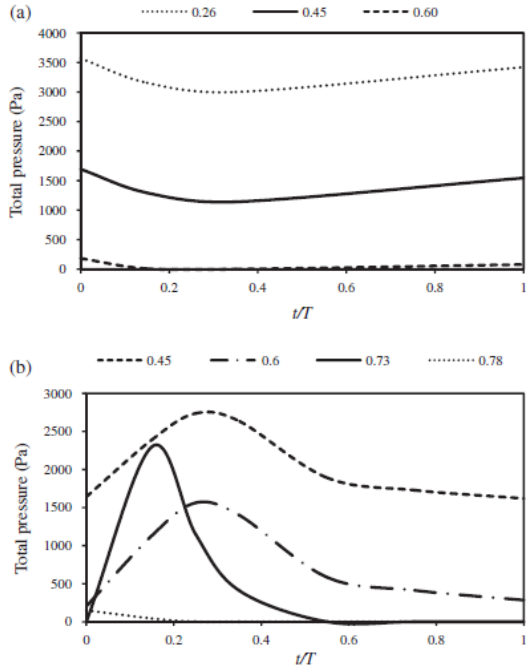
Fig. 12. Time variation of total pressure at different depths (listed in the figure, units are in m) and distances of (a) $x = 20$ m, (b) $x = 25.26$ m.

the pressure distribution is almost hydrostatic, excluding the area near the wave front and crest. Where the wave breaks and collapses, the pressure distribution is remarkably distorted, and far from hydrostatic assumption, especially under the plunging breaker when flow acceleration is no longer negligible. This is mainly due to the creeping motion of the breaking wave, momentum exchange, collision of the breaking wave front onto the flow below, shear flow underneath the free surface and vortices near the wave crest. Therefore, numerical models based on the hydrostatic pressure distribution (e.g., depth-averaged models like the non-linear shallow water equation) are not precise. However, RANS models are able to simulate reasonably details of the flow and turbulence fields. After the wave breaking and further transport into the swash zone, the pressure distribution is more uniform than that in the inner surf zone, but highly turbulent motion and interaction between ingoing and outgoing swashes induce a non-hydrostatic pressure distribution.

Fig. 11 illustrates the vertical distribution of static and total pressures at different times near the breaking point (e.g., $x = 25.26$ m). Panel (a) shows the pressure profiles before passing the wave, in which the total pressure is equal to the static pressure and both of them increase linearly with depth towards the bed. Therefore, at this time, it is close to hydrostatic. On the other hand, it can be concluded from panels b–d that the magnitudes of total pressure at various times differ from the corresponding static pressures, especially in the upper part of water column and near the wave front. At the time of wave breaking and in the surface roller region, the total pressure due to wave breaking is up to three times higher than the static pressure, and also the total pressure for non-breaking waves. This difference at the wave front and inside the
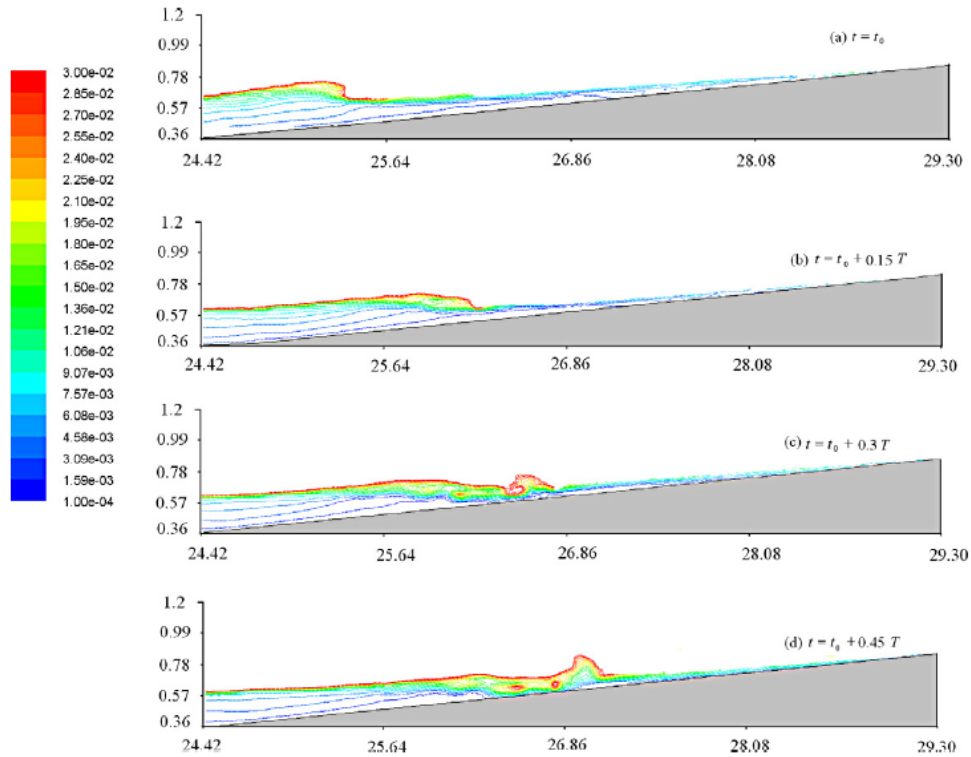

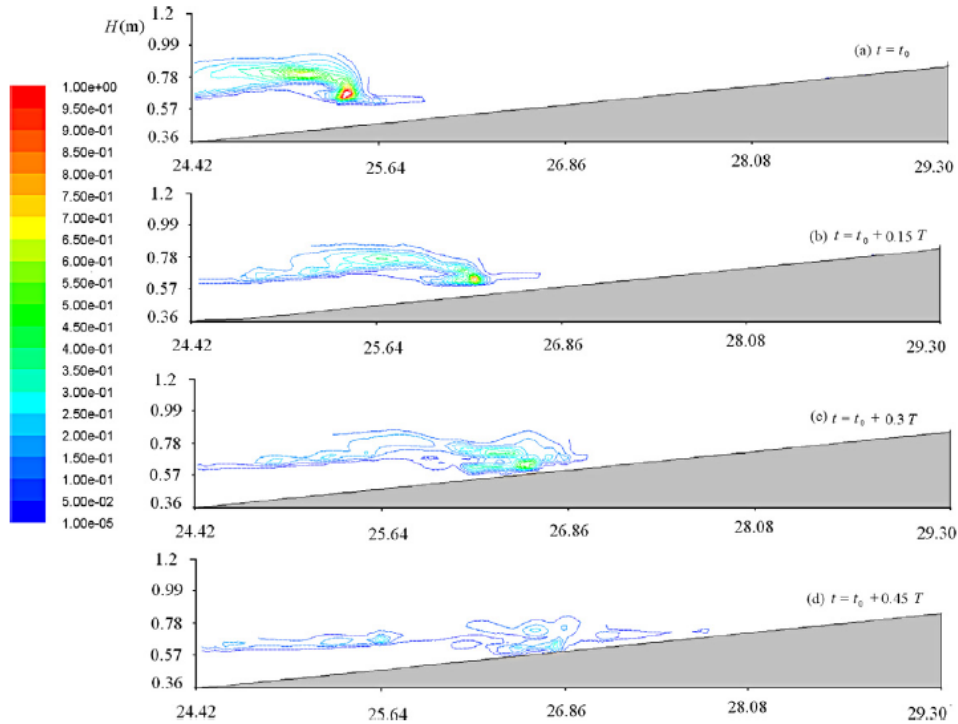**Fig. 13.** Predicted TKE in m² s⁻² by the RNG model.

Fig. 14. Turbulence dissipation rate during the wave motion based on RNG model. Horizontal axis shows the cross-shore distance in m, and the vertical axis shows the vertical distance in m.

convex breaking front reflects the strong horizontal and vertical velocities that exist at the wave face during the breaking process. Pedrozo-Acuña et al. [38] showed that for plunging breakers, the advective acceleration term $w\frac{\partial u}{\partial z}$ gives a significant contribution to the non-hydrostatic pressure gradient. After wave breaking, the difference between total and static pressures decreases until the next wave reaches this point (panel d).

Fig. 12 demonstrates the time variation of total pressure at different depths and two positions ($x = 20$ and 25.26 m). At $x = 20$ m (before wave breaking), it is evident that the pressure decreases with elevation, and that the pressure fluctuates with time during the wave period. Fig. 12(b) shows that, in the lower part of water column, the pressure increased with the depth, while near the breaking area and surface roller, the variation of total pressure during one wave period is considerable. This is due to the fact that the liquid velocity, wave structure and turbulence changes irregularly and, when the wave breaks, the dynamic pressure is high. Total pressure reaches a maximum under the wave front during wave breaking and pressure decays quickly after passage of the wave crest. The dynamic pressure decreases towards the bottom.

3.4. Turbulence characteristics

Fig. 13 shows the time variation of TKE during the wave transformation in the surf and swash zones and also near the free surface. In Fig. 13, as the wave is getting closer to the first breaking point, the wave TKE increases near the free surface. Near the breaking point, the TKE is significant until wave breaks, where it reaches its maximum value. The value of TKE under the wave crest is larger than near the bed and decays noticeably towards it because, in the surf zone, the dominant mechanism generating turbulence is the breaker near the surface roller [20]. After the wave breaking point, TKE decreases towards the shore and is directed landward. It is

obvious that the turbulence production near the bottom is less energetic compared to near the wave free surface boundary. The highest TKE appears to be under the wave crest, near the free surface and behind the wave front. After wave breaking, the turbulence energy is carried away with the accelerated uprush flow and does not spread into the whole flow region. In other words, under plunging waves the onshore advection is more important than diffusion. These findings are consistent with existing understanding of the wave dynamics [20,4]. Generally, the magnitude of TKE in the inner surf zone and in vicinity of wave breaking is higher than in the swash zone; but in the swash zone, due to depth reduction, the TKE appears near the bed. The highly turbulent motion close to the bed in the swash zone causes high bottom shear stress, which would induce high sediment transport in a layer very close to the bed (e.g., the dominant sediment transport mode is sheet flow).

Fig. 14 represents the simulated turbulence dissipation rate during the wave motion based on the RNG turbulence closure model. The distribution of the turbulence dissipation rate is similar to the TKE distribution. In both models, the maximum value of the turbulence dissipation rate occurs in the vicinity of breaking point front. The mixing of air and water in the upper part of the water column dissipates the main part of the TKE before it penetrates downward throughout the water column [18]. The highest dissipation rate also appears under the wave crest and near the free surface. In the collapsing area, as the wave starts to break over the shallow water, both the turbulence production and dissipation begin to increase within the surface roller of the breaking wave. As already noted, the TKE is advected with the wave turbulent motion into the swash zone. Consequently, the generated turbulence is not diffused into the water column beneath the SWL.

Fig. 15 depicts the distribution of turbulent effective viscosity under the wave motion in the cross-shore direction. After wave
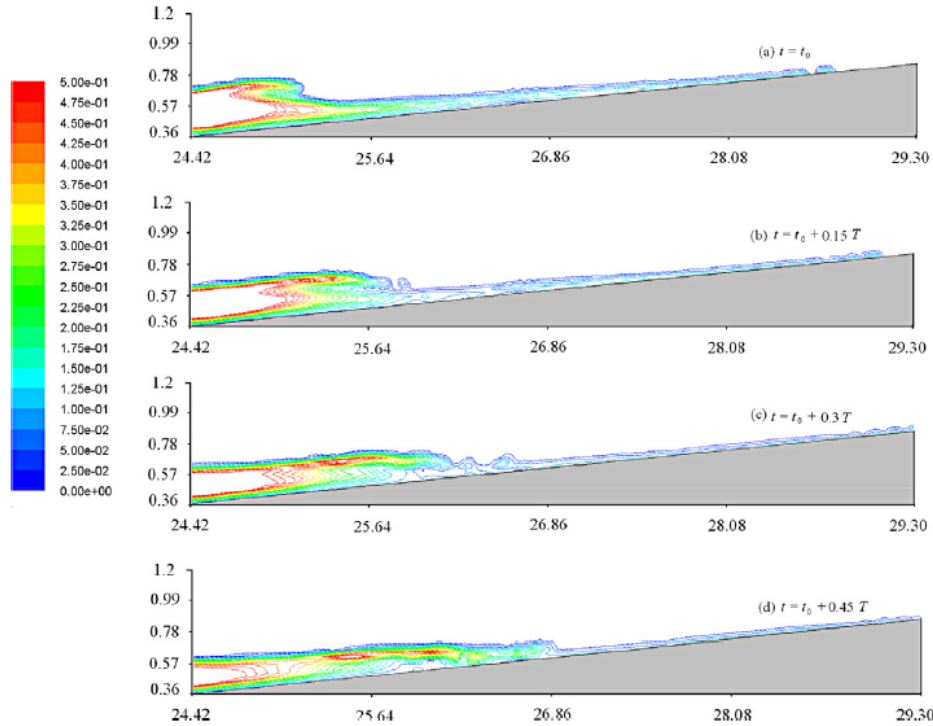
Fig. 15. Simulated effective viscosity during the wave motion based on RNG model. Horizontal axis shows the cross-shore distance in m, and the vertical axis shows the vertical distance in m.

breaking, turbulence is generated at the surface layer. This generated turbulence increases the TKE and produces an increased eddy viscosity [39]. The cross-shore distribution of eddy viscosity is governed by the turbulence dissipation rate and TKE (Eq. (A-3)). The largest eddy viscosity appears to be around the breaking point (same area as the TKE). This maximum is between one and two orders of magnitude larger than that before the breaking point. The eddy viscosity then decreases towards the bottom.

3.5. Turbulence distribution under various wave conditions

In order to investigate the nearshore hydrodynamics subject to the influence of wave characteristics, a suite of numerical experiments was performed. Numerical experiments were run considering two wave periods (1 and 4 s), covering both spilling and plunging breakers, and two wave heights (9 and 12.16 cm) with the previous model setup.

Fig. 16 shows the cross-shore variation of the TKE for waves with $H_0 = 12.16$ cm and wave period of 1, 2 and 4 s. As expected from Eq. (10) the wave period directly influences the breaker types. Galvin [40] pointed out based on observations that if height and beach slope are held constant and the wave period is increased, the breaker type goes from spilling to plunging to collapsing to surging. For the waves with $T = 1$ and 4 s, the surf similarity parameter values are $\zeta = 0.31 < 0.5$ and $\zeta = 1.21 > 0.5$, respectively, which represents (i) a spilling breaker and (ii) a breaker that is between plunging and collapsing. A comparison of these breakers indicates that the TKE under the plunging breaker is much higher in comparison to that under a spilling breaker (Fig. 16). The TKE for spilling is low. This is likely due to the fact that the wave energy is proportional to the wave period, so for the spilling breaker the wave
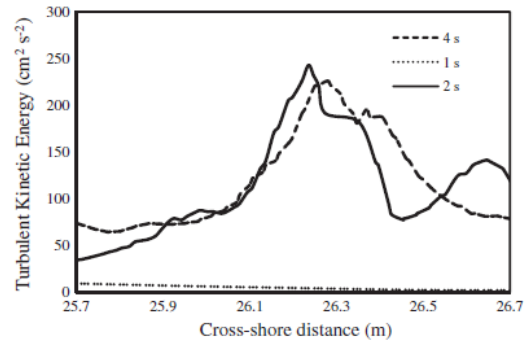

Fig. 16. Cross-shore variation of the TKE for waves with $H_0 = 12.16$ cm and different wave periods (listed in the figure) using the RNG model.

energy is low (period is short). Therefore, turbulent variations are more important in a plunging breaker. The maximum TKE for the spilling breaker happens sooner for the plunging breaker. These results are consistent with the existing findings about different flow hydrodynamics of the spilling and plunging breakers [20]. Furthermore, Fig. 16 shows one peak in the TKE for the wave with $T = 4$ s, which represents one wave breaking, while the wave with $T = 2$ s has two breaking points. For this case, significant TKE is generated in surf zone and is transmitted to the swash zone. The TKE is advected to the swash zone under the collapsing breaker more than that under the plunging breaker.

Fig. 17 depicts the distribution of TKE in the nearshore zone for waves with $T = 2$ s and deep-water wave heights 12, 16 and 9 cm. It
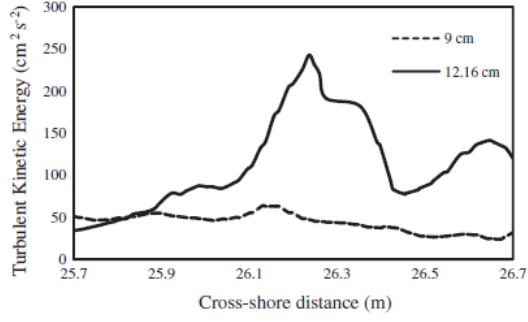
Fig. 17. Distribution of TKE in the nearshore zone for waves with $T = 2$ s and different deep water wave heights (listed in the figure) using the RNG model.

can be observed that the TKE peak moves upward with rising wave height. Generally, in the surf zone, the TKE increases towards the onshore until the breaking points while in the swash zone it decreases in the direction of the maximum uprush. Increasing H_0 causes an increase in momentum exchange, mixing and TKE.

4. Concluding remarks

Beach morphology and sediment transport characteristics depend strongly on the nearshore hydrodynamics and flow patterns, e.g., free surface, velocity and turbulence. In order to investigate the surf/swash zone hydrodynamics including the velocity and turbulence fields, water–air flow in these zones were studied using the two-phase flow framework. The numerical model is based on two-dimensional RANS equations, and the two-phase VOF technique with different turbulent closure models (k–ε, k–ω and RNG). An important feature of the present model is the capability of handling density differences between air and water in the free surface and accounting for the mixing of air and water. The method was verified against the experimental data of Shin and Cox [12] and Shin [31]. The overall comparisons between numerical results and experimental data are satisfactory. The model is suitable for the simulation of water–air mixing flow in the nearshore zone. This non-hydrostatic model is more appropriate than the hydrostatic counterpart since wave breaking plays a crucial role in the nearshore hydrodynamics.

The two-phase-RNG approach outperforms k–ε and k–ω turbulent closure models in terms of prediction capability for surf and swash hydrodynamics. A two-phase flow model supplemented with the RNG turbulence closure model is computationally reasonable and relatively well calibrated for different wave conditions. As a result, the mechanism of wave motion, turbulence, wave breaking, undertow and interaction of water and air in the nearshore zone can be elucidated. The numerical model presented in this study is able to simulate detailed hydrodynamic characteristics in the nearshore area.

Wave motion in the nearshore zone and especially wave breaking naturally induces high curvature and consequently strong vorticity that is 3-D. In addition, waves reach the shore obliquely and induce longshore currents that 2-D models cannot simulate. There is a need for numerical models to investigate the 3-D nearshore hydrodynamics and its interaction with sediment transport and beach profile changes.

Acknowledgements

Appendix A. Turbulence closure models

There are several approaches employed in turbulence modeling coupled with two-phase equations. We present three turbulence closure models that were used in the present study.

A.1. The standard k–ε model

The most popular two-equation turbulence model is k–ε. The equations for TKE (k) and turbulent dissipation rate (ε) are as follows:

$$\frac{\partial k}{\partial t} + \bar{u}_j \frac{\partial k}{\partial x_j} = \frac{\partial}{\partial x_j}\left[\left(\nu + \frac{\nu_t}{\sigma_k}\right)\frac{\partial k}{\partial x_j}\right] - \nu_t\left(\frac{\partial \bar{u}_i}{\partial x_j} + \frac{\partial \bar{u}_j}{\partial x_i}\right)\frac{\partial \bar{u}_i}{\partial x_j} - \varepsilon, \quad \text{and}$$
(A-1)

$$\frac{\partial \varepsilon}{\partial t} + \bar{u}_j \frac{\partial \varepsilon}{\partial x_j} = \frac{\partial}{\partial x_j}\left[\left(\nu + \frac{\nu_t}{\sigma_\varepsilon}\right)\frac{\partial \varepsilon}{\partial x_j}\right] + C_{1\varepsilon}\frac{\varepsilon}{k}\nu_t\left(\frac{\partial \bar{u}_i}{\partial x_j} + \frac{\partial \bar{u}_j}{\partial x_i}\right)\frac{\partial \bar{u}_i}{\partial x_j} - C_{2\varepsilon}\frac{\varepsilon^2}{k},$$
(A-2)

$$\nu_t = C_\mu \frac{k^2}{\varepsilon},$$
(A-3)

in which ν_t is the eddy viscosity and $\sigma_k = 1$, $\sigma_\varepsilon = 1.3$, $C_{1\varepsilon} = 1.44$, $C_{2\varepsilon} = 1.92$, $C_\mu = 0.09$ are empirical constants. These constants have been defined based on experiments with air and water for turbulent shear flows. They have been found to work rather well for a wide range of free shear flows [34].

A.2. The RNG k–ε model [41]

$$\frac{\partial(\rho k)}{\partial t} + \bar{u}_j \frac{\partial(\rho k)}{\partial x_j} = \frac{\partial}{\partial x_j}\left(\alpha_k \mu_{eff} \frac{\partial k}{\partial x_j}\right) + G_k + G_b - \rho\varepsilon - Y_M, \quad \text{and}$$
(A-4)

$$\frac{\partial(\rho\varepsilon)}{\partial t} + \bar{u}_j \frac{\partial(\rho\varepsilon)}{\partial x_j} = \frac{\partial}{\partial x_j}\left(\alpha_k \mu_{eff} \frac{\partial \varepsilon}{\partial x_j}\right) + (G_k + C_{3\varepsilon}G_b)C_{3\varepsilon}\frac{\varepsilon}{k} - C_{4\varepsilon}\rho\frac{\varepsilon^2}{k} - R_\varepsilon,$$
(A-5)

where G_k represents the generation of TKE due to the mean velocity gradients; G_b is the generation of TKE due to buoyancy; Y_M represents the contribution of the fluctuating dilatation in compressible turbulence to the overall dissipation rate; α_k and α_ε are the inverse effective Prandtl numbers; $C_{3\varepsilon} = 1.42$ and $C_{4\varepsilon} = 1.68$ are the empirical constants; and μ_{eff} is the effective viscosity.

A.3. The standard k–ω model

The equations for TKE and specific dissipation rate (ω) are as follows:

$$\frac{\partial(\rho k)}{\partial t} + \bar{u}_j \frac{\partial(\rho k)}{\partial x_j} = \frac{\partial}{\partial x_j}\left(\Gamma_k \frac{\partial k}{\partial x_j}\right) + G_k - Y_k, \quad \text{and}$$
(A-6)

$$\frac{\partial(\rho\omega)}{\partial t} + \bar{u}_j \frac{\partial(\rho\omega)}{\partial x_j} = \frac{\partial}{\partial x_j}\left(\Gamma_\omega \frac{\partial \omega}{\partial x_j}\right) + G_\omega - Y_\omega,$$
(A-7)

where G_ω represents the generation of ω; Γ_k and Γ_ω represent the effective diffusivity of k and ω, respectively; and Y_ω represents the dissipation of ω due to turbulence.

Appendix B. Model performance criteria

In this study, the criteria used for measuring the model performance were the *bias*, the coefficient of determination (R^2), root

mean square error (*RMSE*) and the scatter index (*SI*) that are defined as follows:

$$bias = \frac{1}{N}\sum_{i=1}^{N}(P_i - E_i), \tag{B-1}$$

$$RMSE = \sqrt{\frac{1}{N}\sum_{i=1}^{N}(P_i - E_i)^2}, \tag{B-2}$$

$$SI = \frac{RMSE}{\overline{E}_m} \times 100, \tag{B-3}$$

$$R^2 = \frac{\sum_{i=1}^{N}(E_i - \overline{E}_m)(P_i - \overline{P}_m)}{\left[\sum_{i=1}^{N}(E_i - \overline{E}_m)^2\right]^{\frac{1}{2}}\left[\sum_{i=1}^{N}(P_i - \overline{P}_m)^2\right]^{\frac{1}{2}}}, \tag{B-4}$$

where $\overline{E}_m$ is the experimental mean value; E_i are the experimental values; P_i are the predicted values; and N is the number of observations; on and $\overline{P}_m$ is the predicted mean value.

References

[1] Bakhtyar R, Barry DA, Li L, Jeng D-J, Yeganeh-Bakhtiary A. Modeling sediment transport in the swash zone: a review. Ocean Eng 2009;36:767–83.
[2] Elfrink B, Baldock TE. Hydrodynamics and sediment transport in the swash zone: a review and perspectives. Coast Eng 2002;45:149–67.
[3] Ting FC, Kirby JT. Observation of undertow and turbulence in a laboratory surf zone. Coast Eng 1994;24:51–80.
[4] Ting FC, Kirby JT. Dynamics of surf zone turbulence in a strong plunging breaker. Coast Eng 1995;24:177–204.
[5] Ting FC, Kirby JT. Dynamics of surf zone turbulence in a spilling breaker. Coast Eng 1996;27:131–60.
[6] Fuhrman DR, Madsen PA. Simulation of nonlinear wave run-up with a high-order Boussinesq model. Coast Eng 2008;55:139–54.
[7] Hoque MA, Asano T. Numerical study on wave-induced filtration flow across the beach face and its effects on swash zone sediment transport. Ocean Eng 2007;34:2033–44.
[8] Lin P, Liu PL-F. A numerical study of breaking waves in the surf zone. J Fluid Mech 1998;359:239–64.
[9] Huang ZC, Hsiao SC, Hwung HH, Chang KA. Turbulence and energy dissipations of surf-zone spilling breakers. Coast Eng 2009;56:733–46.
[10] Huang ZC, Hwung HH, Hsiao SC, Chang KA. Laboratory observation of boundary layer flow under spilling breakers in surf zone using particle image velocimetry. Coast Eng 2010;57:343–57.
[11] Sou IM, Cowen EA, Liu PL-F. Evolution of the turbulence structure in the surf and swash zones. J Fluid Mech 2010;644:193–216.
[12] Shin S, Cox D. Laboratory observations of inner surf and swash zone hydrodynamics on a steep slope. Cont Shelf Res 2006;26:561–73.
[13] Bakhtyar R, Ghaheri A, Yeganeh-Bakhtiary A, Barry DA. Process-based model for nearshore hydrodynamics, sediment transport and morphological evolution in the surf and swash zones. Appl Ocean Res 2009;31:44–56.
[14] Hirt CW, Nichols BD. Volume of fluid (VOF) method for the dynamics of free boundaries. J Comp Phys 1981;39:201–25.
[15] Bradford SF. Numerical simulation of surf zone dynamics. J Waterw Port Coast Ocean Eng 2000;126:1–13.
[16] Zhang Q, Liu PL-F. A numerical study of swash flows generated by bores. Coast Eng 2008;55:1113–34.
[17] Christensen ED, Deigaard R. Large eddy simulation of breaking waves. Coast Eng 2001;42:53–86.
[18] Christensen ED. Large eddy simulation of spilling and plunging breakers. Coast Eng 2006;53:463–85.
[19] Zhao Q, Armfield S, Tanimoto K. Numerical simulation of breaking waves by a multi-scale turbulence model. Coast Eng 2004;51:53–80.
[20] Bakhtyar R, Barry DA, Yeganeh-Bakhtiary A, Ghaheri A. Numerical simulation of surf-swash zone motions and turbulent flow. Adv Water Resour 2009;32:250–63.
[21] Bakhtyar R, Yeganeh-Bakhtiary A, Barry DA, Ghaheri A. Two-phase hydrodynamic and sediment transport modeling of wave-generated sheet flow. Adv Water Resour 2009;32:1267–83.
[22] Bakhtyar R, Yeganeh-Bakhtiary A, Barry DA, Ghaheri A. Euler–Euler coupled two-phase flow modeling of sheet flow sediment motion in the nearshore. J Coast Res 2009;SI56:467–71.
[23] Bakhtyar R, Barry DA, Yeganeh-Bakhtiary A, Li L, Parlange J-Y, Sander GC. Numerical simulation of two-phase flow for sediment transport in the inner-surf and swash zones. Adv Water Resour 2010;33:277–90.
[24] Hieu PD, Tanimoto K. A two-phase flow model for simulation of wave transformation in shallow water. In: Proceedings of the fourth international summer symposium. Kyoto: JSCE; 2002. p. 179–82.
[25] Karim MF, Tanimoto K, Hieu PD. Simulation of wave transformation in vertical permeable structure. In: Proceedings of the 13th international offshore and polar engineering conference, Hawaii, USA, vol. 3; 2003. p. 727–33.
[26] Hieu PD, Tanimoto K, Ca VT. Numerical simulation of breaking waves using a two-phase flow model. Appl Math Model 2004;28(11):983–1005.
[27] Lubin P, Vincent S, Abadie S, Caltagiron J-P. Three-dimensional large eddy simulation of air entrainment under plunging breaking waves. Coastal Eng 2006;53(8):631–55.
[28] Hieu PD, Katsutoshi T. Verification of a VOF-based two-phase flow model for wave breaking and wave-structure interactions. Ocean Eng 2006;33(11–12):1565–88.
[29] Wang Z, Zou Q, Reeve D. Simulation of spilling breaking waves using a two-phase flow CFD model. Comput Fluids 2009;38:1995–2005.
[30] Brocchini M, Baldock TE. Recent advances in modeling swash zone dynamics: influence of surf-swash interaction on nearshore hydrodynamics and morphodynamics. Rev Geophys 2008;46:RG3003. doi:10.1029/2006RG000215.
[31] Shin S. Laboratory observations and numerical modeling of inner surf and swash zone hydrodynamics on a steep slope. PhD dissertation. Corvallis: Oregon State University; 2005.
[32] Bachelor GK. An introduction to fluid dynamics. UK, Cambridge: Cambridge University Press; 1967.
[33] Barth TJ, Jespersen D. The design and application of upwind schemes on unstructured meshes. Technical report AIAA-89-0366. In: AIAA 27th aerospace sciences meeting, Reno, Nevada; 1989.
[34] FLUENT incorporated, FLUENT 6.3 user's guide. Lebanon, New Hampshire, USA; 2007.
[35] Battjes JA. Surf similarity. In: Proceedings of the 14th international conference on coastal engineering. New York: ASCE; 1974. p. 466–80.
[36] Wilcox DC. Re-assessment of the scale-determining equation for advanced turbulence models. AIAA J 1988;26:1414–21.
[37] Svendsen IA. Mass flux and undertow in a surf zone. Coast Eng 1984;8:347–65.
[38] Pedrozo-Acuña A, Torres-Freyermuth A, Zou Q-P, Hsu T-J, Reeve DE. Diagnostic investigation of impulsive pressures induced by plunging breakers impinging on gravel beaches. Coast Eng 2010;57:252–66.
[39] Christensen ED, Walstra DJ, Emarat N. Vertical variation of the flow across the surf zone. Coast Eng 2002;45:169–98.
[40] Galvin Jr CJ. Wave breaking in shallow water. In: Meyer RE, editor. Waves on beaches and resulting sediment transport. New York: Academic Press; 1972. p. 413–56.
[41] Yakhot V, Orszag SA. Renormalization group analysis of turbulence, I. Basic theory. J Sci Comput 1986;1:1–51.